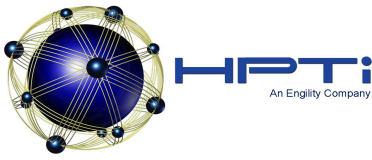


REPORT DOCUMENTATION PAGE			Form Approved OMB No. 0704-0188	
Public reporting burden for this collection of information is estimated to average 1 hour per response, including the time for reviewing instructions, searching existing data sources, gathering and maintaining the data needed, and completing and reviewing this collection of information. Send comments regarding this burden estimate or any other aspect of this collection of information, including suggestions for reducing this burden to Department of Defense, Washington Headquarters Services, Directorate for Information Operations and Reports (0704-0188), 1215 Jefferson Davis Highway, Suite 1204, Arlington, VA 22202-4302. Respondents should be aware that notwithstanding any other provision of law, no person shall be subject to any penalty for failing to comply with a collection of information if it does not display a currently valid OMB control number. PLEASE DO NOT RETURN YOUR FORM TO THE ABOVE ADDRESS.				
1. REPORT DATE (DD-MM-YYYY) 25/08/2015		2. REPORT TYPE Final Technical Report		3. DATES COVERED (From - To) 01/09/2014 - 31/08/2015
4. TITLE AND SUBTITLE Simulation of Structures Exhibiting Instability Under Thermal-Mechanical Transient Loading Final Technical Report			5a. CONTRACT NUMBER GS04T09DBC0017	
			5b. GRANT NUMBER	
			5c. PROGRAM ELEMENT NUMBER	
6. AUTHOR(S) Stanciulescu, Ialina			5d. PROJECT NUMBER BY14-020SP	
			5e. TASK NUMBER	
			5f. WORK UNIT NUMBER	
7. PERFORMING ORGANIZATION NAME(S) AND ADDRESS(ES) High Performance Technologies Innovations LLC 4803 Stonecroft Blvd. Chantilly, VA 20151			8. PERFORMING ORGANIZATION REPORT NUMBER BY14-020SP-D4	
9. SPONSORING / MONITORING AGENCY NAME(S) AND ADDRESS(ES) Department of Defense High Performance Computing Modernization Program Office 10501 Furnace Road Suite 101 Lorton, VA 22079			10. SPONSOR/MONITOR'S ACRONYM(S) HPCMP, PETTT	
			11. SPONSOR/MONITOR'S REPORT NUMBER(S)	
12. DISTRIBUTION / AVAILABILITY STATEMENT DISTRIBUTION A. Approved for public release: distribution unlimited; Case #: 88ABW-2015-4721				
13. SUPPLEMENTARY NOTES				
14. ABSTRACT This document is the Final Technical Report for the PETTT Special Project, BY14-020SP, Simulation of Structures Exhibiting Instability Under Thermal-Mechanical Transient Loading. Slender curved structures such as shallow arches and cylindrical panels are commonly used structural components in aerospace engineering. When these curved structures are subjected to transverse loads, they can be susceptible to snap-through buckling where a structure suddenly jumps from its initial configuration to a remote coexisting equilibrium configuration. Such processes lead to large and frequent stress reversals that can significantly exacerbate the fatigue failure. This report focuses on investigating the static and dynamic snap-through of slender curved structures. The report first presents an analytical method to study the nonlinear static buckling and post-buckling of shallow arches with geometric imperfections. Then an efficient alternative is proposed to quickly determine the dynamic snap-through boundaries of shallow arches and cylindrical panels.				
15. SUBJECT TERMS PETTT, HPC, HPCMP, snap-through, dynamic instabilities, coexisting solution, time integration, numerical stability				
16. SECURITY CLASSIFICATION OF:			17. LIMITATION OF ABSTRACT UU	18. NUMBER OF PAGES 20
a. REPORT Unclassified	b. ABSTRACT Unclassified	c. THIS PAGE Unclassified		
				19b. TELEPHONE NUMBER (include area code) 703-812-8205



Simulation of Structures Exhibiting Instability Under Thermal-Mechanical
Transient Loading

BY14-020SP
Deliverable D4

Final Technical Report

Submitted by
Ilinca Stanciulescu (*Rice University*)
25 August 2015

for
User Productivity Enhancement, Technology Transfer, and Training
(PETTT) Program

High Performance Computing Modernization Program (HPCMP)



Contract No.: GS04T09DBC0017

Government Users/Sponsors/Partners: Thomas Eason (*AFRL/SSC*)

TABLE OF CONTENTS

1	OVERVIEW	1
1.1	Problem of interest.....	1
2	ACCOMPLISHMENTS	1
2.1	Arches with geometric imperfections	1
2.1.1	<i>Equilibrium Equations</i>	2
2.1.2	<i>Buckling Equations</i>	3
2.1.3	<i>Closed-form solutions</i>	4
2.1.4	<i>Application to half-sine arches</i>	5
2.2	Scaling of snap-through boundaries.....	8
2.2.1	<i>A lower-order model for shallow arches</i>	9
2.2.2	<i>Half-sine arches</i>	10
2.2.3	<i>Parabolic arches</i>	13
2.2.4	<i>Cylindrical panels</i>	15
3	SUMMARY	18
4	REFERENCES	18

1 OVERVIEW

This Final Technical Report constitutes the completion of the PETTT Special Project BY14-020SP.

1.1 Problem of Interest

Slender curved structures such as shallow arches and cylindrical panels are commonly used structural components in aerospace engineering. When these curved structures are subjected to transverse loads, they can be susceptible to snap-through buckling where a structure suddenly jumps from its initial configuration to a remote coexisting equilibrium configuration (Figure 1). Such processes lead to large and frequent stress reversals that can significantly exacerbate the fatigue failure [1-6].

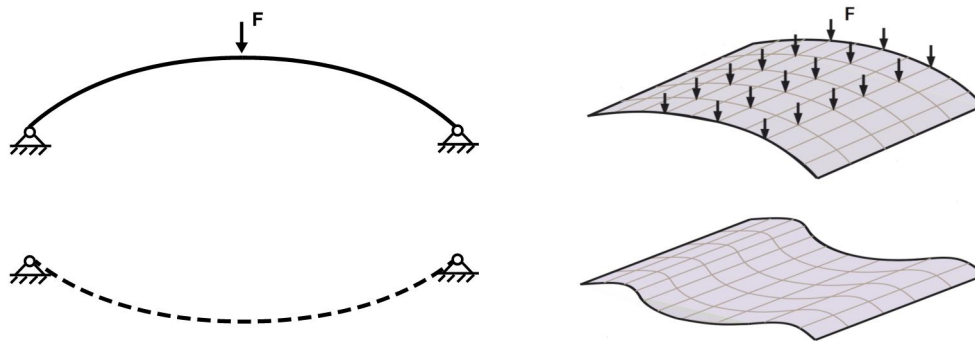


Figure 1. Snap-through buckling

This report focuses on investigating the static and dynamic snap-through of slender curved structures. The report first presents an analytical method to study the nonlinear static buckling and post-buckling of shallow arches with geometric imperfections. Then an efficient alternative is proposed to quickly determine the dynamic snap-through boundaries of shallow arches and cylindrical panels.

2 ACCOMPLISHMENTS

In this section, an analytical model is first presented to analyze the nonlinear stability and remote unconnected equilibrium states of shallow arches with geometric imperfections. The exact solutions of the equilibria and critical loads are obtained. Unlike many previous studies, these solutions can be applied to arbitrary shallow arches with arbitrary geometric imperfections. Then a simple scaling approach is introduced and applied to identify the similarities of snap-through boundaries of half-sine arches, parabolic arches and cylindrical panels.

2.1 Arches with Geometric Imperfections

The nonlinear equilibrium and buckling equations are first derived for the simply supported shallow arch with an arbitrary initial shape and subjected to an arbitrary vertical load f^* (Figure 2).

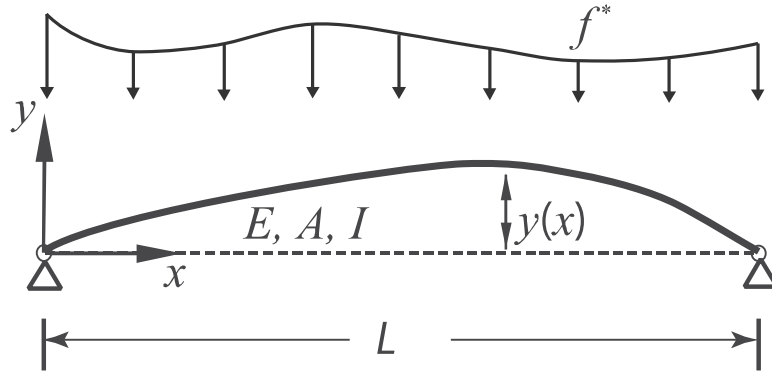


Figure 2. The shallow arch subjected to a transverse load

The material of the arch is assumed to be elastic, isotropic and homogenous. A large displacement Euler Bernoulli beam theory is used to model the nonlinearity. In Figure 2, E represents the Young's modulus; A and I denote the area and moment of inertial of the cross section respectively; L is the horizontal projection of the arch.

2.1.1 Equilibrium Equations

The equilibrium states of shallow arches can be described by the following differential equation:

$$EI(y - y_0)_{,xxxx} - P^* y_{,xx} = f^* \quad (1)$$

Here, y and y_0 are the deformed and initial configurations, the subscript denotes the partial differentiation with respect to the horizontal position, f^* denotes the external load, and P^* represents the axial force that can be calculated as:

$$P^* = \frac{EA}{2L} \int_0^L (y_{,x}^2 - y_{0,x}^2) dx \quad (2)$$

Eqs. (1) and (2) can be written in dimensionless forms as following:

$$(u - u_0)_{,\xi\xi\xi\xi} - pu_{,\xi\xi} - q = 0 \quad (3)$$

$$p = \frac{1}{2\pi} \int_0^\pi (u_{,\xi}^2 - u_{0,\xi}^2) d\xi \quad (4)$$

Here, $(u, u_0) = \frac{1}{r}(y, y_0)$, $\xi = \frac{\pi}{L}x$, $r = \sqrt{\frac{I}{A}}$.

Utilizing the Fourier sine series, u , u_0 and q can be written as:

$$u(\xi) = \sum_1^{\infty} \alpha_n \sin(n\xi), \quad u_0(\xi) = \sum_1^{\infty} \beta_n \sin(n\xi), \quad q = \sum_1^{\infty} q_n \sin(n\xi), \quad (5)$$

where,

$$q_n = \frac{2}{\pi} \int_0^{\pi} q \sin(n\xi) d\xi \quad (6)$$

The nonlinear equilibrium equations can then be obtained by substituting Eqs. (5) and (6) into Eqs. (3) and (4):

$$R_n = 0 \quad (\alpha_n - \beta_n)n^4 + pn^2\alpha_n - q_n = 0, \quad n = 1, 2, \dots \quad (7)$$

$$p = \sum_{k=1}^{\infty} \frac{(\alpha_k^2 - \beta_k^2)k^2}{4} \quad (8)$$

2.1.2 Buckling Equations

The tangent stiffness of the system becomes singular when the structure loses stability. The tangent stiffness matrix of the system can be obtained from Eqs. (7) and (8):

$$K_{nm} = \frac{\partial R_n}{\partial \alpha_m} = \frac{n^2 m^2}{2} \alpha_n \alpha_m + n^2(n^2 + p)\delta_{nm}, \quad n, m = 1, 2, \dots \quad (9)$$

where δ_{nm} is the Kronecker delta function. When the tangent stiffness matrix is singular, its determinant equals zero. Therefore, the buckling equation can be derived as:

$$\det K_{nm} = \prod_{k=1}^{\infty} \gamma_{kk} + \sum_{n=1}^{\infty} (\alpha_n^2 \prod_{\substack{k=1 \\ k \neq n}}^{\infty} \gamma_{kk}) = 0 \quad (10)$$

$$\text{Here, } \gamma_{nm} = \frac{2n^2(n^2 + p)\delta_{nm}}{n^2 m^2}.$$

2.1.3 Closed-form Solutions

In this part, the closed-form solutions to the equilibrium and buckling equations are derived for shallow arches subjected to a concentrated load at the midspan. Without truncating the Fourier sine series, the expressions of exact solutions are obtained.

2.1.3.1 Equilibrium States

Express the dimensionless transverse load q with respect to the loading parameter λ as

$q = -\frac{\pi}{2} \lambda \delta(\xi - \frac{\pi}{2})$. Here, $\frac{\pi}{2}$ is a scaling factor for the convenience of following derivations, and the loading parameter λ is positive when the external load is in the negative y direction (Figure 2). Therefore, the load series q_n can be obtained as:

$$\begin{aligned} q_{2i+1} &= (-1)^{i+1} \lambda, & i &= 0, 1, 2, \dots \\ q_{2i} &= 0, & i &= 1, 2, \dots \end{aligned} \quad (11)$$

Substituting the load series q_n into the Eq. (7) the mode coefficients α_n then satisfy:

$$\begin{aligned} (2i+1)^2 ((2i+1)^2 + p) \alpha_{2i+1} &= (-1)^{i+1} \lambda + \beta_{2i+1} (2i+1)^4, & i &= 0, 1, \dots \\ ((2i)^2 + p) \alpha_{2i} &= \beta_{2i} (2i)^2, & i &= 1, 2, \dots \end{aligned} \quad (12)$$

Therefore, the mode coefficients for the equilibrium states can be solved as

$$\begin{aligned} \alpha_{2i+1} &= \frac{(-1)^{i+1} \lambda + \beta_{2i+1} (2i+1)^4}{(2i+1)^2 ((2i+1)^2 + p)}, & i &= 0, 1, \dots \\ \alpha_{2i} &= \frac{\beta_{2i} (2i)^2}{((2i)^2 + p)}, & i &= 1, 2, \dots \end{aligned} \quad (13)$$

Substituting α_n into the Eq. (8), a quadratic function of the loading parameter λ with respect to the non-dimensional axial load p is obtained:

$$A(p)_{2,2} \lambda^2 + B(p)_{2,2} \lambda + C(p) = 0 \quad (14)$$

Here, $A(p)_{M,N}$, $B(p)_{M,N}$ and $C(p)$ are defined as following

$$A(p)_{M,N} = \sum_{i=0}^{\infty} \frac{1}{(2i+1)^M ((2i+1)^2 + P)^N} \quad (15)$$

$$B(p)_{M,N} = \sum_{i=0}^{\infty} \frac{(-1)^{i+1} 2\beta_{2i+1} (2i+1)^M}{((2i+1)^2 + P)^N} \quad (16)$$

$$C(p) = \sum_{i=1}^{\infty} \frac{\beta_i^2 i^6}{(i^2 + p)^2} - \sum_{i=1}^{\infty} \beta_i^2 i^2 - 4p \quad (17)$$

The solutions of the loading parameter λ are

$$\lambda = \frac{-B(p)_{2,2} \pm \sqrt{(B(p)_{2,2})^2 - 4A(p)_{2,2} C(p)}}{2A(p)_{2,2}} \quad (18)$$

The vertical displacement at the midspan can be obtained by substituting α_n to Eq. (5):

$$\Delta u_{mid} = u_0(\pi/2) - u(\pi/2) = A(p)_{2,1} \lambda + B(p)_{2,1}/2 + \sum_{i=0}^{\infty} (-1)^i \beta_{2i+1} \quad (19)$$

Eqs. (18) and (19) can be utilized to obtain the equilibrium states for different values of p .

2.1.3.2 Critical Loads

When $\beta_{2i} \neq 0$, for all i , we obtain that $p \neq -(2j)^2$ and hence no bifurcated equilibrium branch exists. Therefore, Eq. (10) is satisfied only at limit points and can be further simplified to:

$$1 + \sum_{n=1}^{\infty} \frac{\alpha_n^2}{\gamma_{nn}} = 0 \quad (20)$$

Substituting α_n into Eq. (20), the limit-point buckling load can be obtained as:

$$A(p)_{2,3} \lambda^2 + B(p)_{2,3} \lambda + \sum_{i=1}^{\infty} \frac{\beta_i^2 i^6}{(i^2 + p)^3} + 2 = 0 \quad (21)$$

2.1.4 Application to Half-sine Arches

In this part, the previous derivations are applied to half-sine arches with an initial dimensionless height $\beta_1 = h$ and asymmetric geometric imperfections $\beta_{2i} = e_{2i} h$ ($i = 1, 2, 3$). Since the imperfection mode coefficients β_{2i} appear with a quadratic form in all related expressions, the sign of the coefficients e_{2i} does not influence the results and only positive values of e_{2i} are considered in the following study. To investigate the effect of the first three imperfection modes, the non-dimensional height of the perfect arch is chosen as $h = 13.5$. This value is chosen to ensure that at least three pairs of bifurcation paths exist for the perfect structure. Note that the

physical rise-to-span ratio of the arch is equal to hr/L . Therefore, the dimensionless height $h = 13.5$ represents shallow arches when the value of r/L is small. The analytical results are compared with the finite element analysis (FEA), which uses a physical rise-to-span ratio that is 0.0065 when $h = 13.5$.

2.1.4.1 Equilibrium States

Figure 3 shows the equilibrium states represented in the parameter space $(\Delta u_{mid}, \lambda)$ for the perfect arch with $h = 13.5$ and the imperfect arch with $e_2 = 0.03$, $e_4 = 0.005$ and $e_6 = 0.001$. The solid and dashed lines represent the primary and bifurcated equilibrium states obtained from Eqs. (18) and (19). The circles and squares denote the primary and bifurcated equilibrium states obtained from the FEA. All finite element simulations are performed with the large-deformation Euler-Bernoulli beam element in the Finite Element Analysis Program (FEAP) [7]. The numerical procedure introduced in [8] is adopted to obtain the bifurcated equilibrium states in FEA.

Figure 3a shows that the perfect arch with $h=13.5$ has a complex continuous primary equilibrium path with multiple loops and three different bifurcated equilibrium paths. On these equilibrium paths, 12 critical points exist, including six limit points (locations with horizontal tangents, L_1 - L_6) and six bifurcation points (locations where the primary and bifurcated paths intersect, B_1 - B_6). The results obtained from the analytical solutions and the FEA match well. When the arch has a multiple-mode imperfection with non-zero values for all coefficients e_2 , e_4 and e_6 (Figure 3b), all bifurcated equilibrium paths, which exist for the perfect arch, disappear and six more limit points appear instead. Unlike the perfect structure, there are a large group of remote unconnected equilibrium states, represented by gray solid lines in Figure 3b, which cannot be obtained by the FEA if a proper perturbation is not performed. It is in fact difficult to identify whether the equilibrium states are connected or not for the imperfect arch when they are presented in the space of $(\Delta u_{mid}, \lambda)$. An alternative way to represent the equilibrium states will be introduced.

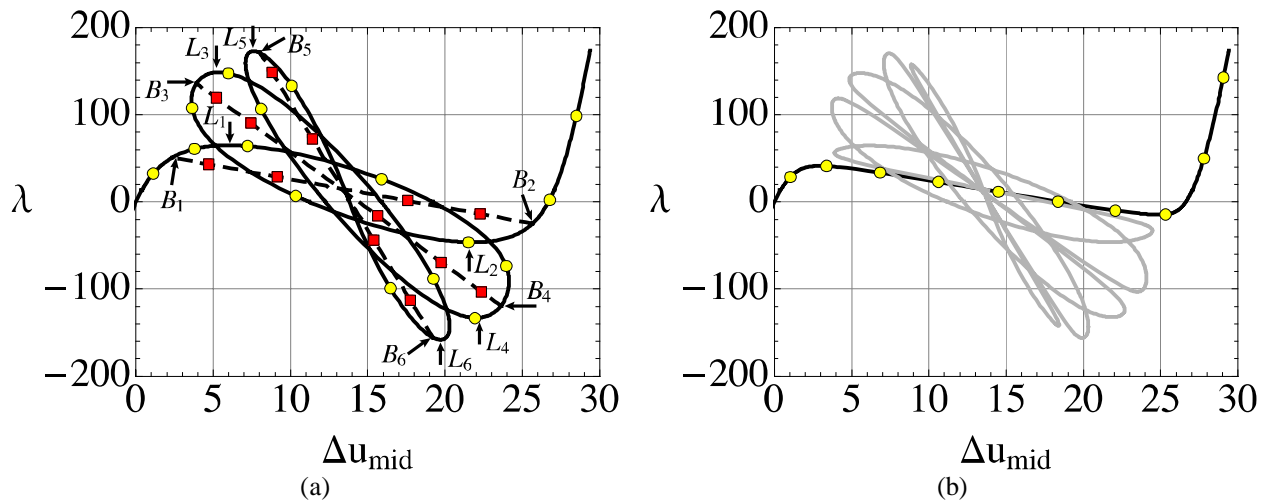


Figure 3. The equilibrium states of half-sine arches represented in the space of $(\Delta u_{mid}, \lambda)$: (a) No imperfection, (b) $e_2 = 0.03$, $e_4 = 0.005$, and $e_6 = 0.001$.

Since the parameter space $(\Delta u_{mid}, \lambda)$ does not give a clear illustration of the equilibrium states of the imperfect arch, it is recommended to represent the equilibrium states by projecting them into the space of the axial load p and the external loading parameter λ . It is observed that this representation of the equilibrium states is very effective in describing the equilibrium states and critical points. Figure 4 shows the same equilibrium states that are plotted in Figure 3. Here, the primary and bifurcated equilibrium states obtained from the proposed formulas are also denoted as solid and dashed curves respectively. The circles and squares again represent the primary and bifurcated equilibrium states obtained by the FEA without initial perturbation. In the parameter space (p, λ) (Figure 4), the limit point can be identified from the local maximum or minimum with zero tangent (L_1 - L_6 in Figure 4a) while the bifurcation point can be identified as the location where the primary and bifurcated paths intersect (B_1 - B_6 in Figure 4a). In addition, it can be clearly seen from Figure 4b that a small imperfection of the mode $\sin(2i\xi)$ ($e_{2i} \neq 0$) makes the bifurcated path of this mode ($\sin(2i\xi)$) disappear and the primary equilibrium states split at the location $p = -4i^2$. This split generates one more pair of limit points and one group of remote unconnected equilibrium states (gray curves) that can include looping paths with multiple limit points.

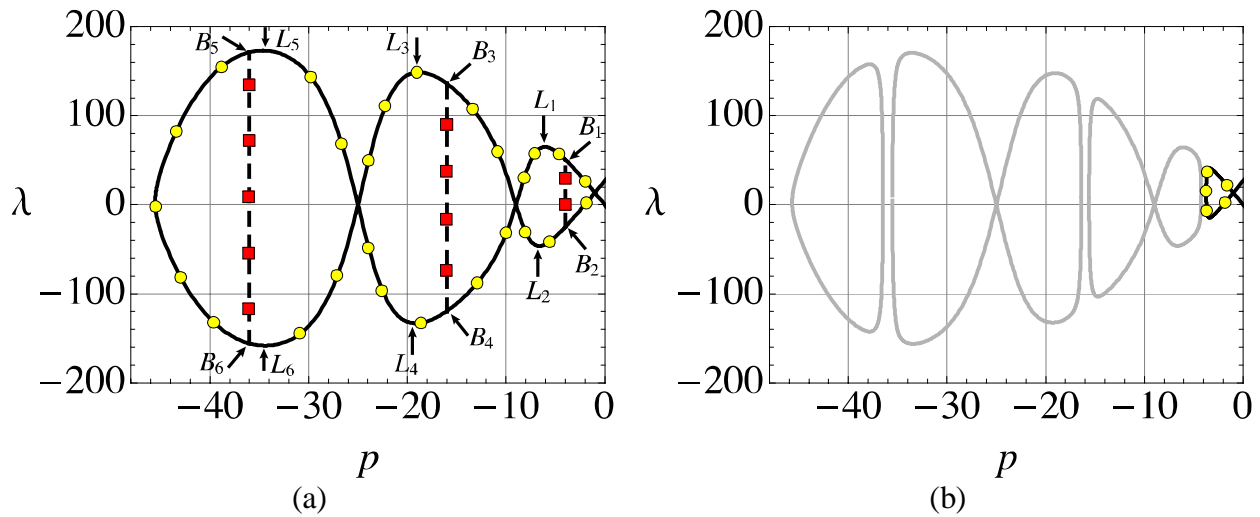


Figure 4. The equilibrium states of half-sine arches represented in the space of (p, λ) : (a) No imperfection, (b) $e_2 = 0.03$, $e_4 = 0.005$, and $e_6 = 0.001$.

2.1.4.2 Critical Loads

In this part, the influence of the multiple-mode imperfection on all critical loads including those of the remote unconnected equilibrium is investigated. From Figure 4, it can be observed that two pairs of critical points exist for $-(2i+1)^2 \leq p \leq -(2i-1)^2$ where $i = 1, 2, 3$. In the following section, the ranges $-9 \leq p \leq -1$, $-9 \leq p \leq -1$, and $-9 \leq p \leq -1$ will be referred to as first, second and third ranges respectively.

Figure 5 shows the variation of the critical loads with respect to the multiple-mode imperfection. The solid lines (black and gray) represent the limit loads obtained from the analytical expressions. Among these results, the gray curves denote the limit loads of the remote

unconnected equilibria. The circles represent the limit loads obtained from the FEA by performing multiple simulations. In this case, all six pairs of critical points are limit loads and five of them are from the remote unconnected equilibria. When the multiple-mode imperfection e increases, the limit loads in all three ranges decrease. The limit loads in the second and third ranges (Figure 5b and 5c) vary much faster than those in the first range (Figure 5a).

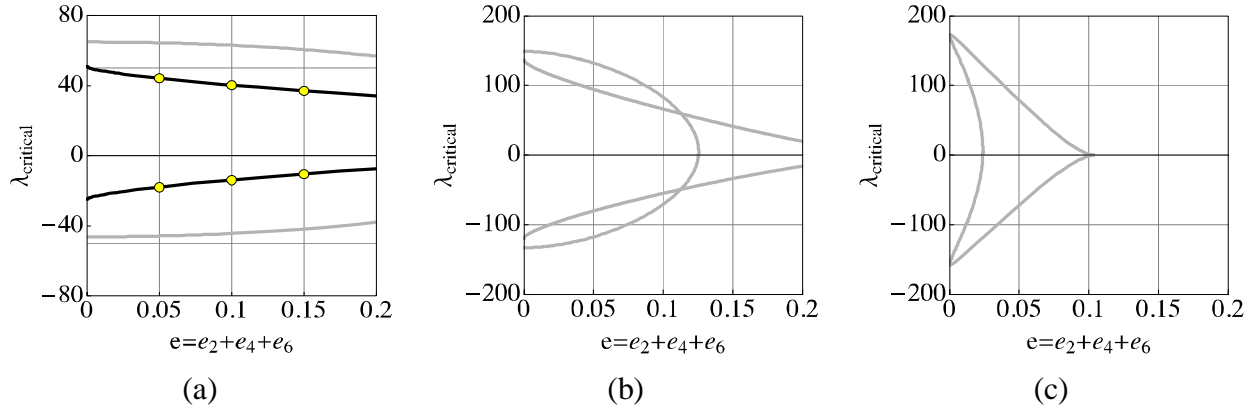


Figure 5. The critical loads of half-sine arches with multiple-mode imperfection $e = e_2 + e_4 + e_6$ where $e_2 = e_4 = e_6 = e/3$: (a) $-9 \leq p \leq -1$, (b) $-25 \leq p \leq -9$ and (c) $-49 \leq p \leq -25$.

2.2 Scaling of Snap-through Boundaries

To reveal the relationship between different dynamic snap-through boundaries, a simple scaling approach is proposed: the forcing amplitudes are scaled by the static buckling load of the structure and the forcing frequencies are scaled by the linear natural frequency of the first symmetric mode. A schematic representation is shown in Figure 6. Here λ represents the dynamic forcing amplitudes and λ_{cr} denotes the static buckling load; ω represents the excitation forcing frequencies and ω_{sym1} is the linear natural frequency of the first symmetric mode.

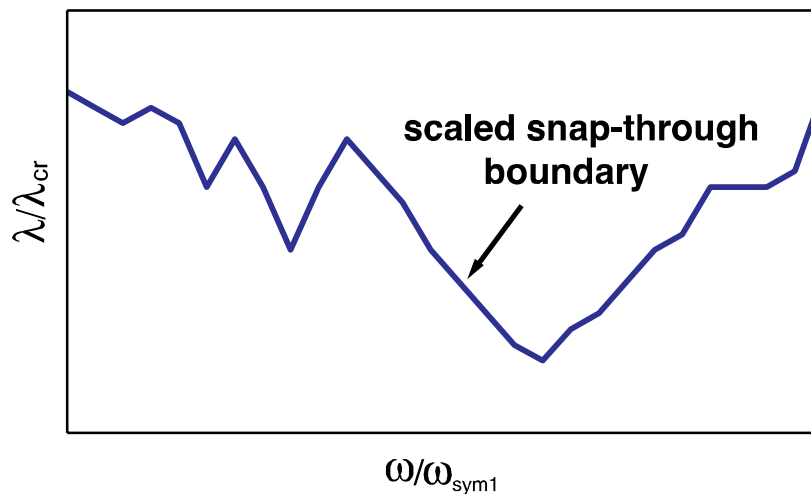


Figure 6. Scaled snap-through boundaries of six half-sine arc

2.2.1 A lower-order model for shallow arches

The equation of motion is first derived for a simply supported shallow arch subjected to a point load at midspan (Figure 7). The material of the arch is assumed to be elastic, isotropic and homogenous. A large displacement Euler Bernoulli beam theory is adopted to model the geometric nonlinearity. In Figure 7, ρ denotes the density; E represents the Young's modulus; A and I denote the area and moment of inertial of the cross section respectively; L is the horizontal projection of the arch.

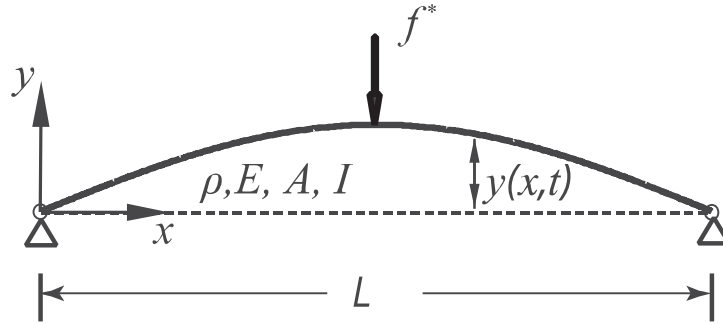


Figure 7. A simply supported shallow arch subjected to a point load at its midspan

The differential equation describing the motion of the arch is as follows:

$$\rho A y_{,tt} + EI(y - y_0)_{,xxxx} - P^* y_{,xx} = f^* \delta^*(x - \frac{L}{2}) \quad (22)$$

Where, y and y_0 are the deformed and initial configurations, the subscripts “,t” and “,x” denote the partial differentiation with respect to the time and horizontal position, f^* denotes the external load, $\delta^*(x)$ is a dimensional Dirac delta function, and P^* represents the axial force that can be calculated as:

$$P^* = \frac{EA}{2L} \int_0^L (y_{,x}^2 - y_{0,x}^2) dx \quad (23)$$

Eqs. (22) and (23) can be transferred into the dimensionless forms as following:

$$y_{,\tau\tau} + (u - u_0)_{,\xi\xi\xi\xi} - p u_{,\xi\xi} = q \delta(\xi - \frac{\pi}{2}) \quad (24)$$

$$p = \frac{1}{2\pi} \int_0^\pi (u_{,\xi}^2 - u_{0,\xi}^2) d\xi \quad (25)$$

Here, $(u, u_0) = \frac{1}{r}(y, y_0)$, $\xi = \frac{\pi}{L}x$, $r = \sqrt{\frac{I}{A}}$, $\tau = \sqrt{\frac{E}{\rho}} \frac{\pi^2 r}{L^2} t$, and $q = \frac{f^* L^3}{\pi^3 E I r}$.

Utilizing the Fourier sine series, u , u_0 and $q\delta(\xi - \frac{\pi}{2})$ can be written as:

$$u(\xi) = \sum_1^\infty \alpha_n \sin(n\xi), \quad u_0(\xi) = \sum_1^\infty \beta_n \sin(n\xi), \quad q = \sum_1^\infty q_n \sin(n\xi), \quad (26)$$

where,

$$q_n = \frac{2}{\pi} \int_0^\pi q \delta(\xi - \frac{\pi}{2}) \sin(n\xi) d\xi \quad (27)$$

Let the external load q be written in terms of the loading parameter λ as $q = -\frac{\pi}{2}\lambda$. Here, $\frac{\pi}{2}$ is a scaling factor for the convenience of following derivations, and λ is positive when the applied load is in the negative y direction (Figure 7). Therefore, the load coefficients q_n is

$$\begin{aligned} q_{2i-1} &= (-1)^i \lambda \quad i = 1, 2, \dots \\ q_{2i} &= 0 \quad i = 1, 2, \dots \end{aligned} \quad (28)$$

The equations of motion can then be obtained by substituting Eq. (26) into Eq. (24):

$$\alpha_{n,\tau\tau} + (\alpha_n - \beta_n)n^4 + pn^2\alpha_n = q_n, \quad n = 1, 2, \dots \quad (29)$$

2.2.2 Half-sine Arches

For a half-sine arch with an initial rise h , the mode coefficients of the initial configuration $\beta_1 = h$ and $\beta_k = 0$ ($k > 1$). Before the transient analysis, it is useful to perform the static buckling analysis to obtain the static buckling loads that will be used in the scaling of dynamic forcing amplitudes. The equilibrium and static buckling equations can be derived from Eq. (7) by neglecting the inertial effect terms $\alpha_{n,\tau\tau}$.

Figure 8 shows the equilibrium paths of half-sine arches with six representative rises. The solid and dashed curves represent the primary and secondary equilibrium states obtained from the lower-order model respectively. The circles and squares denote the primary and secondary equilibrium states obtained from the FEA. These arches can be classified into three groups. For the first group (Figure 8a and 8b), one pair of limit points exists on the equilibrium path. The

arches with these two rises exhibit limit point buckling and the limit point buckling load will be used for scaling the dynamic forcing amplitude. For the second group (Figure 8c and 8d), one pair of bifurcated path exists after the first limit point. The arches in this case still exhibit limit point buckling. For the third group (Figure 8e and 8f), the bifurcation buckling occurs before the first limit point, and the bifurcation buckling loads will be used for the scaling.

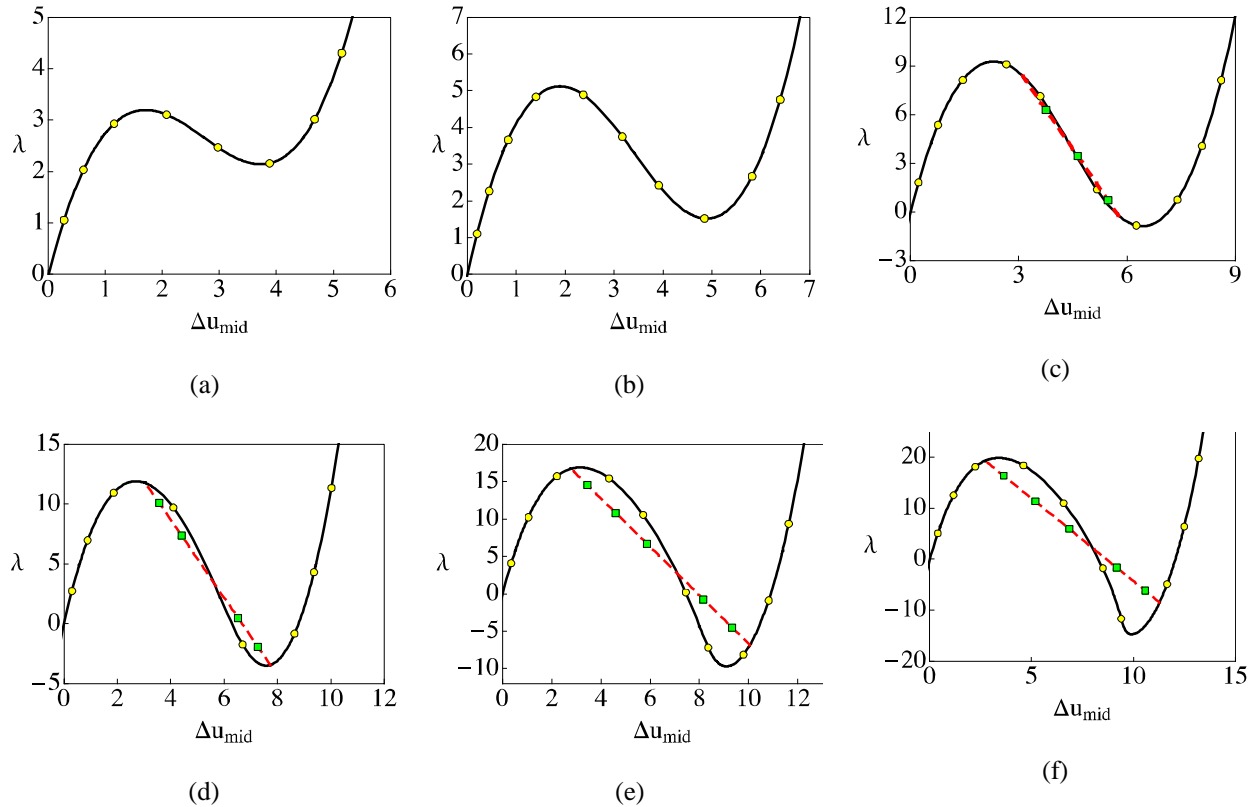


Figure 8. Equilibrium paths of half-sine arches with six different rises: (a) $h=2.67$, (b) $h=3.33$, (c) $h=4.27$, (d) $h=4.53$, (e) $h=5.20$, (f) $h=5.60$.

Figure 9 shows the linear natural frequencies of the first symmetric and asymmetric modes of half-sine arches with different initial rises. The solid and dashed lines represent the frequencies of the first symmetric and asymmetric modes for different rises obtained from the lower order model. The square markers denote the frequencies obtained from the finite element analysis for the six rises just discussed ($h=2.67, 3.33, 4.27, 4.53, 5.20$ and 5.60). It can be observed that the frequency of the first symmetric mode (ω_{sym1}) is much smaller than the frequency of the first asymmetric mode (ω_{asym1}) for very small rises. When the rise of the arch becomes larger, the frequency of the first symmetric mode (ω_{sym1}) also becomes larger, but the frequency of the first asymmetric mode (ω_{asym1}) barely changes. The frequencies of the first symmetric mode (ω_{sym1}) will be used for scaling the excitation forcing frequencies.

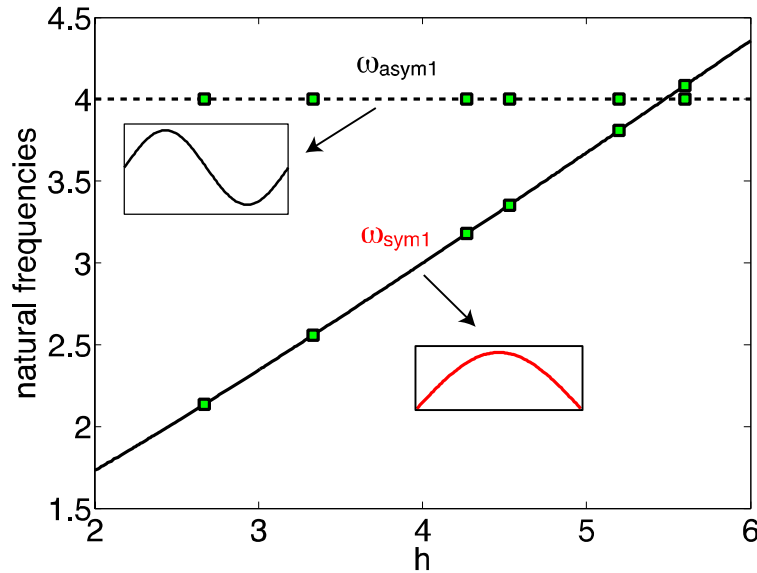


Figure 9. Linear natural frequencies of the first symmetric and asymmetric modes of half-sine arches with different initial rises

In the transient analysis, the harmonic load $\lambda(\tau) = P \sin(\omega\tau)$ is considered. Here, P is the forcing amplitude and ω is the forcing frequency. Since interest is focused on the cases that the dynamic snap-through load is smaller than the static buckling load, the forcing amplitude P is varied from 0 to the static buckling load. The forcing frequency is chosen between 0 and the value where the dynamic buckling load equals to the static buckling load.

The scaled snap-through boundaries of these half-sine arches are shown in Figure 10. It can be seen that all these snap-through boundaries have a very similar V shape with zigzags in certain frequency ranges. For a very low forcing frequency (close to zero), the scaled dynamic buckling load is equal to one, which is as expected since the dynamic effect in this case is very small and the dynamic buckling load should be equal to the static buckling load. It can also be identified that the lowest scaled dynamic buckling loads of all arches appear at almost the same scaled frequency that is smaller than one. This indicates that these shallow arches have a softening nonlinearity with respect to the first symmetric mode, which is also as expected. Moreover, all these snap-through boundaries after scaling almost exactly overlap. With this finding, the snap-through boundaries of half-sine arches with other rises within the range $2.67 \leq h \leq 5.60$ can be quickly estimated from any one of these available boundaries without running any additional transient simulation.

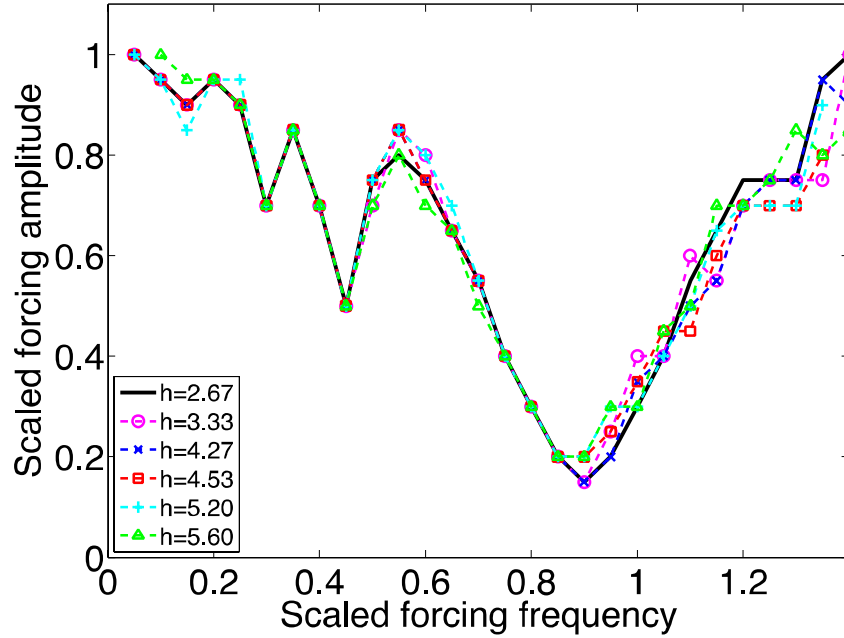


Figure 10. Scaled snap-through boundaries of six half-sine arches

2.2.3 Parabolic Arches

For a parabolic arch with an initial rise h , the mode coefficients of the initial configuration are as follows:

$$\beta_{(2i-1)} = \frac{32h}{\pi^3 (2i-1)^3}, \quad i = 1, 2, 3, \dots \quad (30)$$

$$\beta_{2i} = 0, \quad i = 1, 2, 3, \dots$$

Figure 11 shows the equilibrium states of six parabolic arches with different rises ($h=2.63, 3.31, 4.37, 4.75, 5.65$ and 6.17). The solid and dashed curves represent the primary and secondary equilibrium states obtained from the lower-order model respectively. The circles and squares denote the primary and secondary equilibrium states obtained from the FEA. The parabolic arch (Figure 11) has similar buckling behavior as those of the half-sine arch (Figure 8).

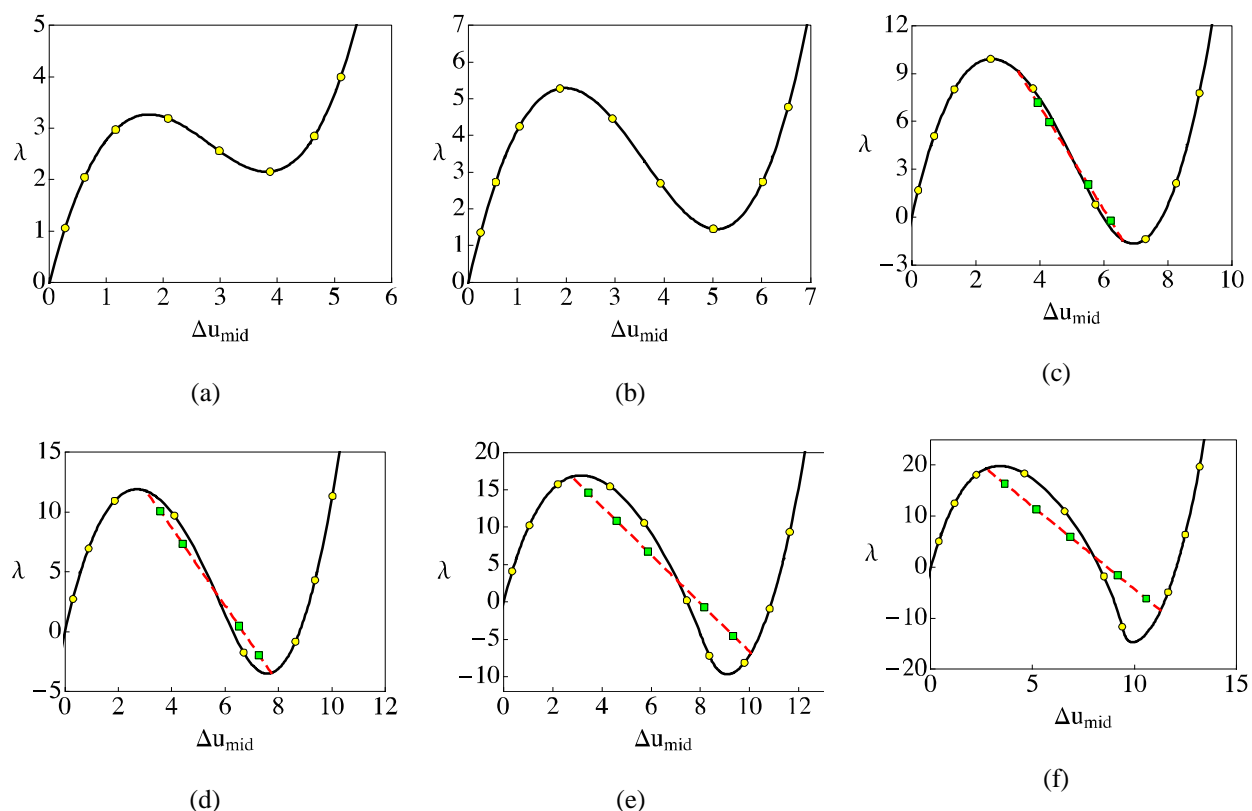


Figure 11. Equilibrium paths of parabolic arches with six different rises: (a) $h=2.63$, (b) $h=3.31$, (c) $h=4.37$, (d) $h=4.75$, (e) $h=5.65$, (f) $h=6.17$.

Utilizing the same scaling approach, the scaled snap-through boundaries of these parabolic arches are shown in Figure 12. These scaled snap-through boundaries can again approximate each other.

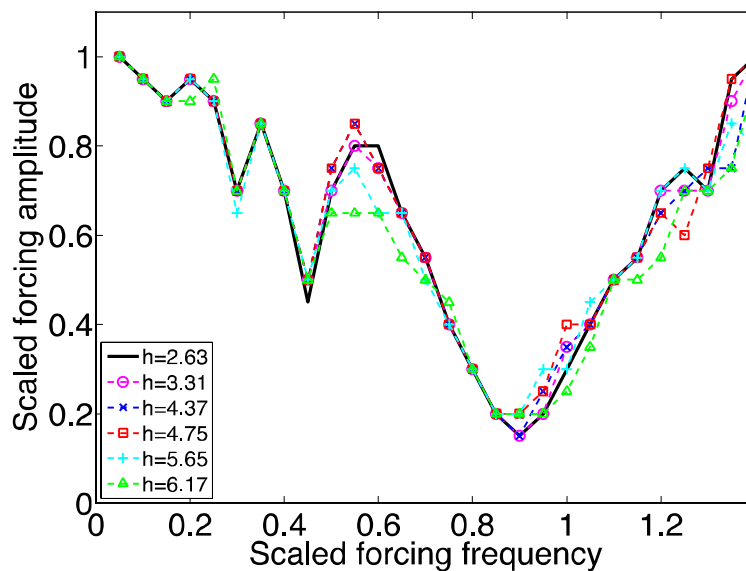


Figure 12. Scaled snap-through boundaries of parabolic arches

2.2.4 Cylindrical Panels

In this section, the proposed scaling approach is applied to cylindrical panels that have higher dimensions than arches. The cylindrical panel considered here is subjected to a uniformly distributed load in the vertical direction. The two straight longitudinal edges are simply supported and the two curved circumferential edges are free. The material and geometric parameters are shown in Figure 13.

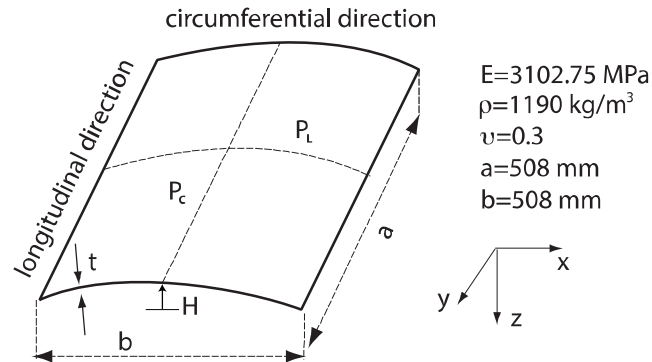


Figure 13. The cylindrical panel

Figure 14 shows the equilibrium paths of four cylindrical panels with different rises. The black solid line represents the primary equilibrium states. The circle markers denote the limit points while other three types of markers represent the bifurcated equilibrium paths. Unlike the shallow arch, cylindrical panels have two more bifurcated equilibrium paths whose corresponding bifurcation buckling mode shapes are shown in Figure 14d.

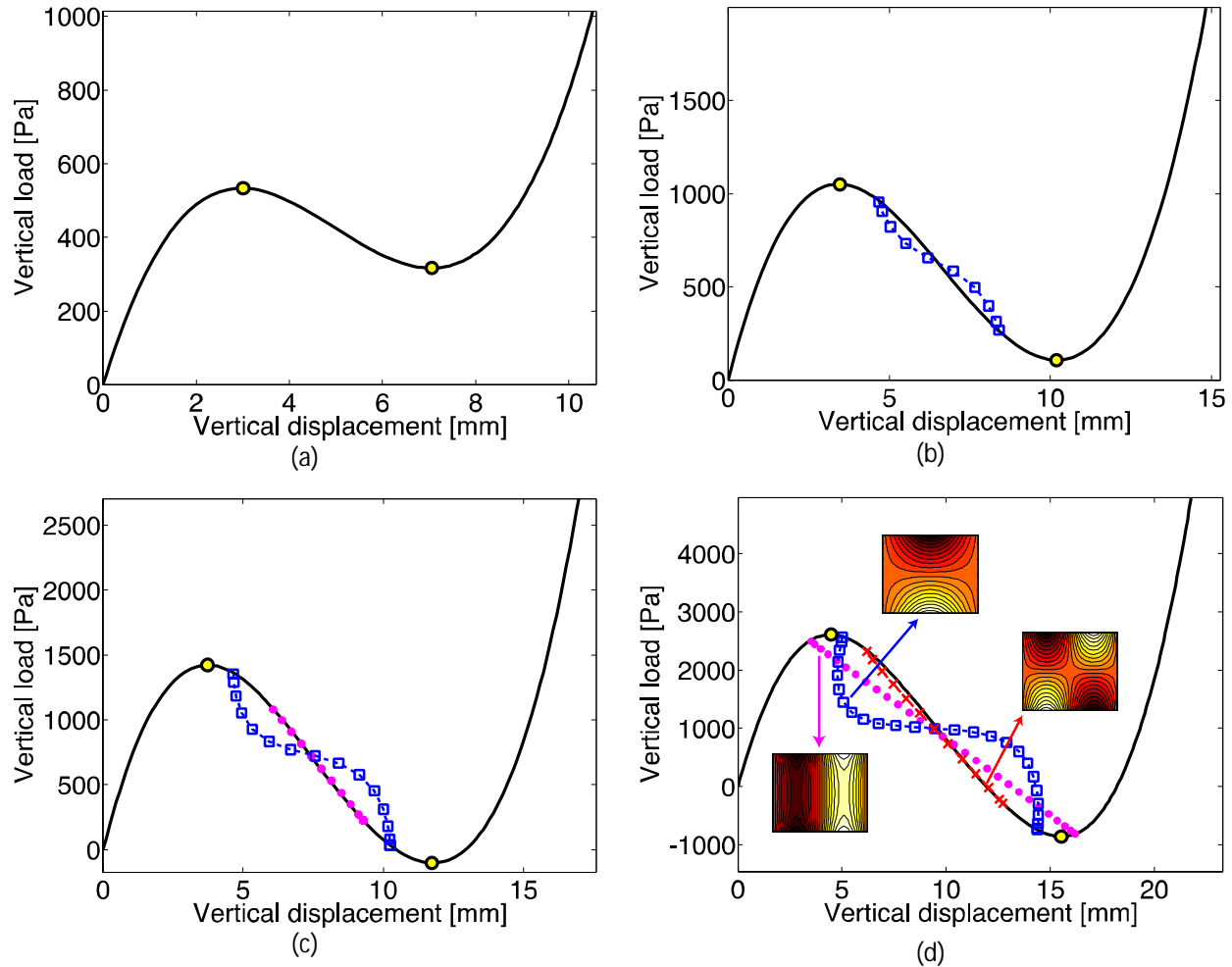


Figure 14. Equilibrium paths of cylindrical panels with four different rises: (a) $H=5.08$ mm, (b) $H=6.86$ mm, (c) $H=7.75$ mm, (d) $H=9.78$ mm.

Utilizing the same scaling method, the scaled snap-through boundaries of cylindrical panels with four different initial rises are shown in Figure 15. These scaled boundaries are again approximately the same. Moreover, it can be seen that the scaled snap-through boundaries of the cylindrical panels are also similar to the boundaries of the half-sine or parabolic arches.

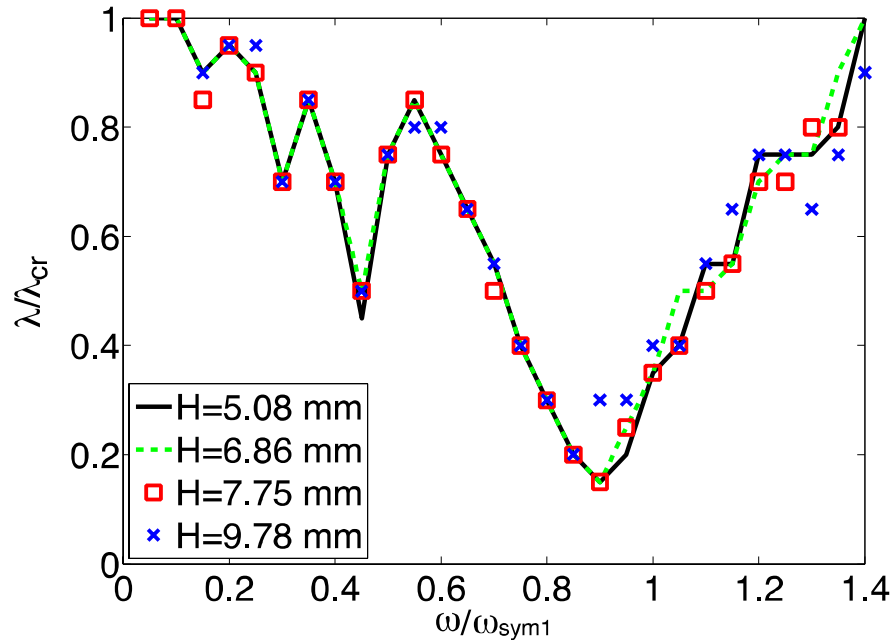


Figure 15. Scaled snap-through boundaries of four different cylindrical panels

Figure 16 shows all scaled snap-through boundaries of these curved structures discussed. The black, red and blue lines represent the boundaries of half-sine arches, parabolic arches, and cylindrical panels respectively. It can be seen that all these boundaries can approximate each other, especially for the forcing frequencies that are smaller than the dominant resonance frequency. This useful identification indicates that the snap-through boundaries of cylindrical panels can be estimated from the boundaries of shallow arches, which usually require much less computational costs than performing that calculation for a panel.

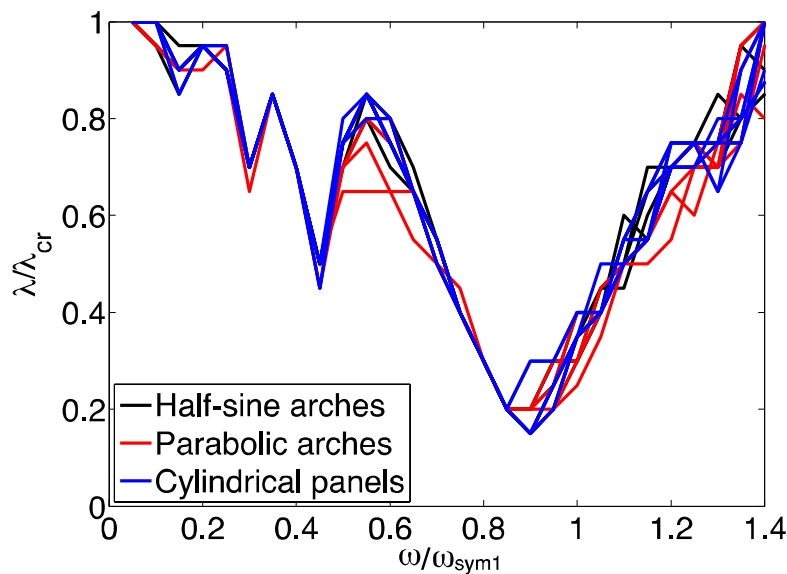


Figure 16. All scaled snap-through boundaries

3 SUMMARY

The work summarized in this final report has two main components:

- (1) An analytical method is proposed to study the nonlinear static stability and remote unconnected equilibria of shallow arches with geometric imperfections. The exact solutions of the equilibria and critical loads are obtained. Unlike many previous studies, these solutions can be applied to arbitrary shallow arches with arbitrary geometric imperfections. It is found that slightly imperfect arches have multiple remote unconnected equilibria that cannot be obtained in experiments or using finite element simulations if a proper perturbation is not performed. The formulas to directly calculate the critical loads are also derived.
- (2) An efficient alternative is presented to quickly determine the dynamic snap-through boundaries of slender curved structures with different geometries, shapes and types. A simple scaling approach is proposed and it identifies very useful similarities of different dynamic snap-through boundaries. With these identified features, other snap-through boundaries of similar structures with different geometries or even the boundaries of different types of structures can be quickly estimated without running any additional transient simulations.

4 REFERENCES

- [1] B. Clarkson, Review of sonic fatigue technology, NASA Technical Report, 1994
- [2] S. Suresh, Fatigue of materials, Cambridge University Press, 1998.
- [3] L. Virgin, Vibration of axially loaded structures, Cambridge University Press, 2007.
- [4] A. Przekoo and S. A. Rizzi, Dynamic snap-through of thin-walled structures by a reduced-order model, AIAA Journal, 45 (10) (2007) 2510-2519.
- [5] Y. Chandra, I. Stanciulescu, L. N. Virgin, T. G. Eason, and S. M. Spottswood, A numerical investigation of snap-through in a shallow arch-like mode. Journal of Sound and Vibration 332. 10 (2013): 2532-2548.
- [6] Y. Chandra, Transient behavior of curved structures, Doctoral Thesis, Rice University, 2013.
- [7] R.L. Taylor, FEAP-Finite Element Analysis Program, University of California, Berkeley, 2014, URL <<http://www.ce.berkeley.edu/projects/feap/>>.
- [8] Y. Zhou, W. Chang, and I. Stanciulescu. Non-linear stability and remote unconnected equilibria of shallow arches with asymmetric geometric imperfections. International Journal of Non-Linear Mechanics 77 (2015): 1-11.